

Machine Learning Predicts Failure in Sandstone Analog using Critical Point Indicators

Harsh Biren Vora and Julia K. Morgan

Department of Earth, Environmental, and Planetary Sciences, Rice University, Houston, TX

Contents of this File:

Text S1 to S4

Figures S1 to S16

Tables S1 to S4

Introduction:

This supporting document includes eight parts:

1. Geomechanical Calibration of Sandstone Model [Text S1, Fig. S1, Fig. S2, Fig. S3; Table S1; Table S2]
2. Calculation of Acoustic Energy and Seismic Moment to derive b-value [Text S2; Fig. S4; Fig. S5; Fig S6; Fig. S7]
3. Calculation of Fractal Dimension [Text S3; Fig. S8]
4. Effect of Confining Pressure on Deformation Indicators [Fig. S9; Fig. S10; Fig. S11; Fig. S12; Fig. S13]
5. Details of Multilayer Perceptron [Text S4; Fig. S14; Fig. S15]
6. Regression Performance of Multilayer Perceptron [Fig. S16]
7. Relative Importance of Neural Network Inputs for Time-to-Failure predictions [Table S3]
8. Relative Importance of Neural Network Inputs for Stress-to-Failure predictions [Table S4]

Text S1: Micromechanical Parameters and Calibration of Bulk Rock Behavior

For this study, we must develop a synthetic analog for sandstone. We do so by carrying out numerical experiments using a range of micromechanical properties assigned to assemblage particles, then comparing the behavior of the synthetic material to the mechanical responses of the intended physical material. The microparameters are adjusted iteratively to improve fit of the modeled and natural behaviors. The process of retroactive adjustment of micromechanical parameters of a Discrete Element model has been successfully used to replicate numerical analogs for sandstone [Vora and Morgan, 2019; Wang et al., 2008; Cook et al., 2004; Wang and Tonon, 2009]. The initial micromechanical parameters used for the sandstone model were geomechanical properties of quartz from Cook et al. [2004]. We calibrated the macroscopic Young's Modulus, Poisson's Ratio and Unconfined Compressive Strength based on the unconfined mechanical behavior of Berea sandstone observed in the laboratory [Bobich, 2005]. In addition, we calibrated Mohr-Coulomb Cohesion and Angle of Internal Friction of our synthetic materials to replicate the confined mechanical behavior of sandstone observed in the laboratory [Schellart, 2000].

Sample volume, boundary stresses and particle positions through time are used to calculate bulk scale properties during biaxial experiments [Fig. S1b]. Boundary stresses of the biaxial domain are calculated along the vertical platens and horizontal membranes, by summing the forces of the particles along each surface and scaling that sum by the surface area [Fig. S1b]. Platen and membrane stresses correspond to the maximum and minimum principal stress, S_1 and S_3 , respectively. Membrane stresses are maintained at a specified confining pressure. The displacement of the platens is used to calculate axial strain (ϵ_a).

Calibration of Young's Modulus (E): The experimental value of Young's Modulus is 8 GPa for Berea Sandstone [Bobich, 2005]. The bulk Young's Modulus in our models is primarily influenced by the Young's Modulus of Particles (E_p), which is controlled by the input elastic microparameters of particles, G_p and ν_p [Vora and Morgan, 2019]. We derive a slightly lower Young's Modulus of 6.48×10^9 Pa for Berea Sandstone [Fig. S2], attained using values of 2.90×10^{10} Pa and 0.33 for G_p and ν_p , respectively

[Table S1]. Experimental values of Young's Modulus of Berea sandstone increase from 8 GPa at confining pressure of 0 MPa to 16.66 MPa at confining pressure of 50 MPa [Bobich, 2005]. We calculate an increase in Young's Modulus from 5.28 GPa to 10.42 GPa as confining pressure is increased from 0 MPa to 45 MPa on calibrated models of sandstone. Thus, although the calibrated values of confined and unconfined Young's Modulus in our sandstone models are a bit lower than experimentally derived values, they lie within desired range [Bobich, 2005].

Calibration of Poisson's Ratio (ν): Experimental values of unconfined Poisson's Ratio is 0.33 for Berea sandstone [Hart and Wang, 1995]. The bulk Poisson's Ratio of our DEM materials show direct correlation with the assigned Poisson's ratio of individual particles (ν_p). Since individual particles of our models cannot fragment during deformation experiments, the elastic deformation of our individual particles must mirror the bulk experimental elastic deformation character of constituent particles, quartz for sandstone. The experimentally derived Poisson's ratio for quartz ranges from 0.19 – 0.29. We employ a particle Poisson's Ratio (ν_p) of 0.33 [Table S1] in our sandstone models to attain a bulk unconfined Poisson's Ratio of 0.29 in our sandstone model [Table S2]. We calculate a decline in bulk Poisson's Ratio from 0.29 to 0.20 as confining pressure is increased from 0 MPa to 50 MPa on calibrated sandstone models. Thus, the calibrated values of confined and unconfined Poisson's ratio in our sandstone models also lie within range of experimentally derived values [Hart and Wang, 1995].

Calibration of Unconfined Compressive Strength (UCS): Experimental value of UCS is 95 MPa for Berea Sandstone [Bobich, 2005]. The bulk UCS in our models is primarily influenced by the tensile strength of bonds (T_b) and Cohesion of bonds (C_b). The bond strengths, T_b and C_b influence the energy required to break bonds in tensile and shear modes, respectively. Scholtès and Donzé [2013] suggest that assigned values of T_b and C_b must have a ratio equal to bulk UCS/TS , where TS is the tensile strength of the rock, to ensure that micromechanical processes reflect the bulk geomechanical behavior of the rock. In this study, we maintain a T_b/C_b ratios of 10 for our sandstone model [Bobich, 2005]. The UCS shows a direct correlation with T_b and C_b , properties that are adjusted to obtain the best fit to the experimental values,

also obeying the guidelines of Scholtès and Donzé [2013]. We attain a UCS of 89.37×10^6 Pa for our sandstone model [Fig. S2; Table S2] by employing values of 3.00×10^7 Pa and 3.00×10^8 Pa for T_b and C_b respectively [Table S1].

Calibration of Mohr-Coulomb Cohesion (C) and coefficient of internal friction (μ): After attaining the desired values of bulk E , ν and UCS , confined compression tests are conducted to attain the desired Mohr-Coulomb behavior (C and μ). Experimental values of C and μ are 26.10 MPa and 0.49 for Berea Sandstone, respectively [Schellart, 2000]. The coefficient of internal friction is derived from the slope of the Mohr-Coulomb failure envelope. The interparticle friction (μ_p) is adjusted incrementally to attain the best fit to the bulk compressive behavior of Berea Sandstone. We employ μ_p of 0.4 for our sandstone models [Table S2] to attain desired Mohr-Coulomb behavior [Fig. S3]. The Mohr-Coulomb failure envelope of our sandstone model is,

$$\tau = 0.44\sigma_n + 28.03 \quad , \quad (S1)$$

where τ is the shear stress and σ_n is the normal stress on the sample. Thus, through retroactive adjustment of micromechanical parameters we calibrate the bulk properties of our sandstone model to experimental datasets of Berea Sandstone [Table S2].

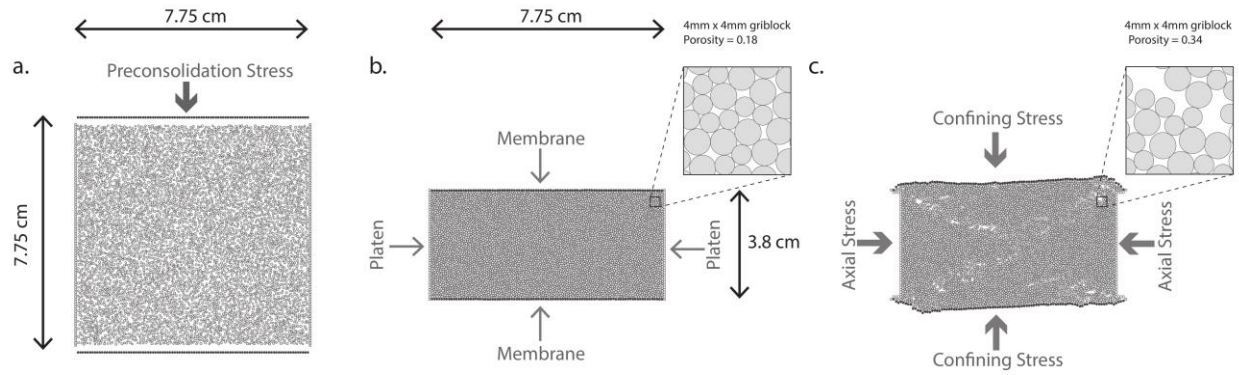
89 **Table S1: Microparameters used to construct analog sandstone model.**

Micromechanical Parameter	Sandstone Model
Young's Modulus of Bonds (E_b) <i>GPa</i>	0.2
Shear Modulus of Bonds (G_b) <i>GPa</i>	0.5
σ_c/σ_t	10
Tensile Strength of Bonds (T_b) <i>MPa</i>	30
Cohesion of Bonds (C_b) <i>MPa</i>	300
Shear Modulus of Particles (G_p) <i>GPa</i>	29
Poisson's Ratio of Particles (ν_p)	0.33
Interparticle friction (μ_p)	0.4

90

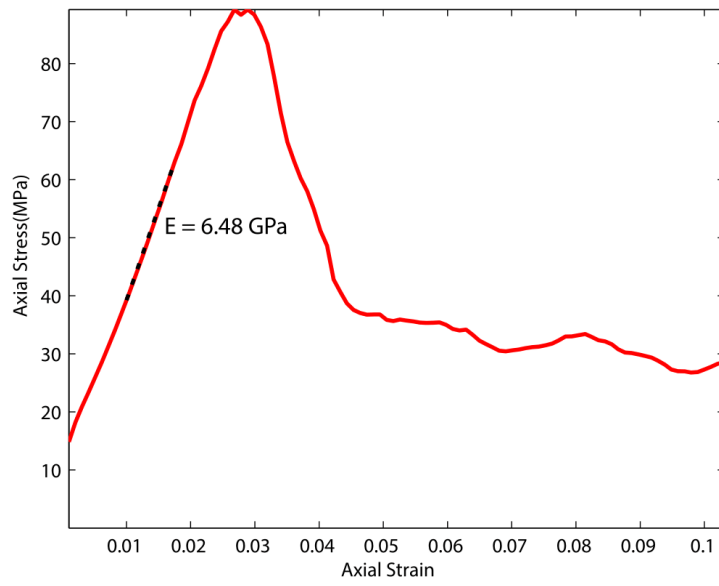
91 **Table S2: Macromechanical behavior of sandstone model (calibrated for Berea Sandstone).**

Macromechanical Property	Model Values for Sandstone Analog	Experimental Values for Berea Sandstone
Unconfined Compressive Strength (UCS) <i>MPa</i>	89.37	95.00
Young's Modulus (E) <i>GPa</i>	6.48	8.00
Poisson's Ratio (ν)	0.29	0.33
Mohr-Coulomb Cohesion (C) <i>MPa</i>	28.03	26.10
Mohr Coulomb Slope (μ)	0.44	0.49



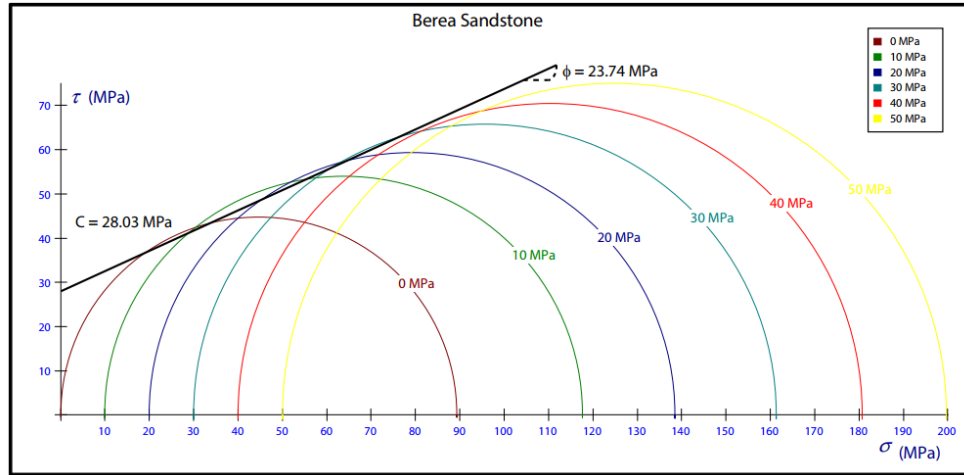
92

93 *Figure S1: Particle distribution and growth of microcracks and associated porosity in sandstone model*
 94 *during biaxial compression test under confining pressure of 15 MPa (a) during preconsolidation, (b) at*
 95 *time of 0 seconds, and (c) time of 1200 seconds. Reproduced from Vora and Morgan [2019].*



96

97 *Figure S2: Unconfined macromechanical behavior of the DEM material calibrated for this study.*
98 *Numerical experiment presented here was carried out under 0 MPa confining pressure.*



99

100 *Figure S3: Mohr-Coulomb properties of calibrated DEM material used in this study. Berea Sandstone*
 101 *model has a cohesion of 28.03 MPa and an angle of internal friction of 23.74 degrees.*

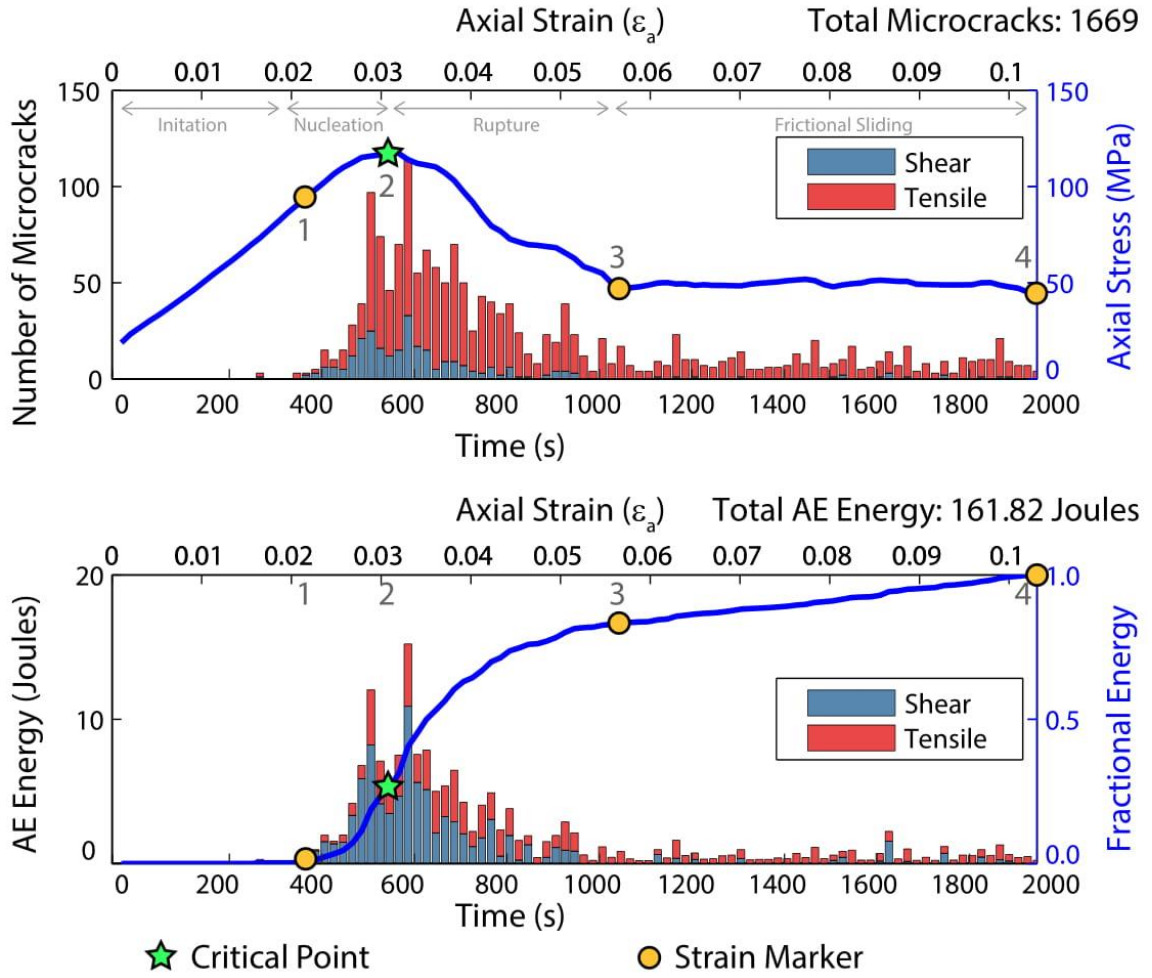
102 **Text S2: Acoustic Energy and Seismic Moment Calculation**

103 **Text S2a: Calculation of Acoustic Energy associated with microcracking (bond failure)**

104 The fracture energy associated with each microcrack is calculated as

$$105 \quad W_{frac} = \left(\frac{1}{2C_f} \right) \sigma_{cf}^2 v_f \quad , \quad (S2)$$

106 where W_{frac} is the energy associated with an individual micro-fracture (J), C_f is the elastic modulus of the
107 bond broken (Pa), σ_{cf} is the stress at failure of the bond broken (Pa) and v_f is the volume of microcrack
108 (m^3) [Tang and Kaiser, 1998]. We define the reference volume of each microcrack (v_f) as half of the total
109 volume of the two particles bounding the broken bond. If the microcrack fails in shear, C_f takes the value
110 of shear modulus of the bond (G_b); if the microcrack fails in tension, C_f takes the value of Young's
111 modulus of the bond (E_b). We assume that acoustic energy (AE_{energy}) released during microcracking is
112 10% of fracture energy, in accordance with estimates of radiated elastic energy during fracture growth
113 [Kanamori and Rivera, 2006; Madden et al., 2017]. The calculated AE_{energy} is documented as a function of
114 time [Fig. S4].



115

116 *Figure S4: Evolution of microcracking and acoustic energy in the sandstone model during biaxial*
 117 *compression test under confining pressure of 10 MPa. (a) Applied axial stress and microcracking in shear*
 118 *and tensile modes as a function of time and axial strain: Deformation stages 1-4 correspond to time of 400*
 119 *s, 720 s, 1200 s and 1800 s, complementing the microcrack distributions in Fig. 1. (b) Spatial distribution*
 120 *of shear and tensile microcracks corresponding to deformation markers 1-4 during the biaxial experiment.*
 121 *(c) Evolution of acoustic energy from microcrack formation in shear and tensile modes as a function of*
 122 *time.*

Text S2b: Spatio-Temporal clustering of Acoustic Energy and Calculation of Seismic Moment

We calculate the moment magnitude (M) associated with the energy of each microcrack [Kanamori, 1983] as

$$M = \frac{2}{3} \log_{10} AE_{energy} - 2.9 \quad . \quad (S3)$$

Due to the narrow range of grain size distribution in our models, the energy associated with microcrack formation, corresponding to individual bond breakage events, also falls into a narrow range. To correct for the narrow range of grain size distribution, we implement a spatial and temporal clustering algorithm developed by Hazzard and Young [2000]. Each time a bond breaks, energy is released, and seismic source information is calculated using Eq. S2. However, each bond breakage event in our models releases approximately the same amount of energy and seismic moment because of the narrow particle size distribution in our models [Fig. S5a]. This is not the case for real earthquakes and AE , where magnitudes exhibit a larger range that follow a power-law frequency-magnitude distribution [Lockner, 1993]. It is therefore postulated that microcracks occurring close together in space and time may be a part of the same macro rupturing event. This is a realistic assumption, as it is known that most seismic events in the field are made up of smaller scale ruptures [Scholz, 1968] and that shear fractures generally grow at a finite velocity [Madariaga, 1976]. Thus, we implement the spatio-temporal clustering algorithm for microcracks developed by Hazzard and Young [2000] for correct moment magnitude calculation of AE events [Fig. S6].

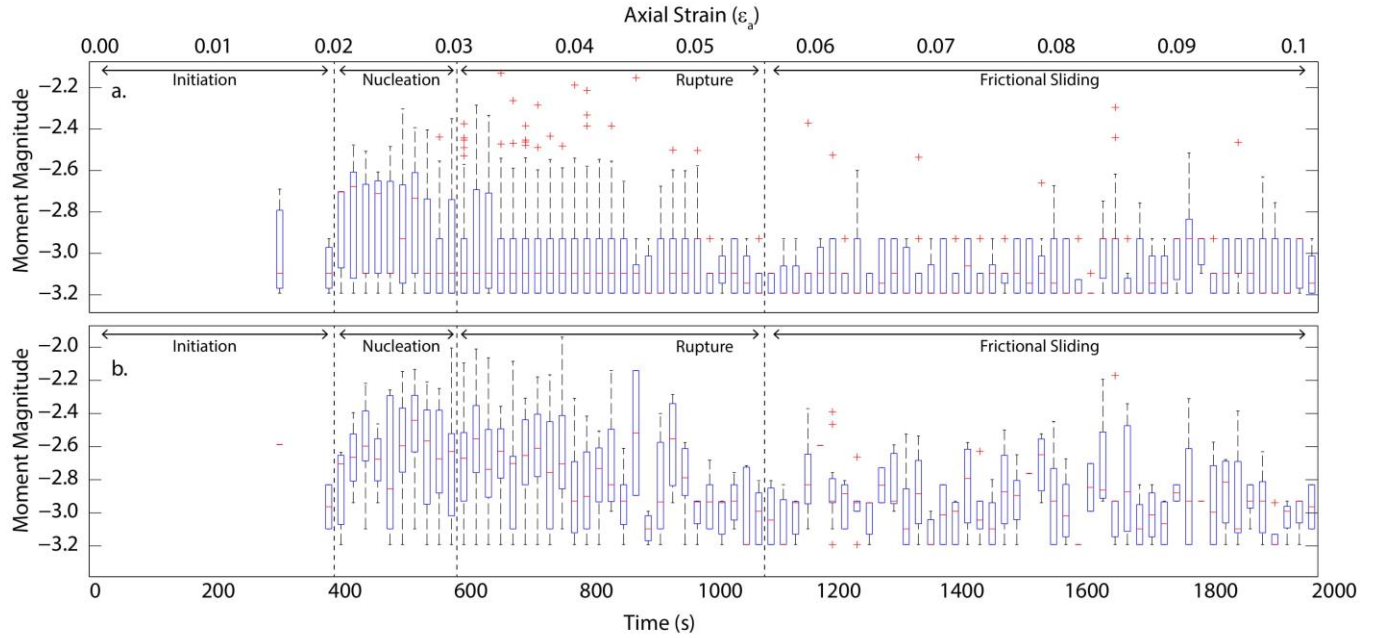


Figure S5: Range of seismic moments from (a) individual microcracks and (b) clustered macrocracks. On each box, the central mark indicates the median, and the bottom and top edges of the box indicate the 25th and 75th percentiles, respectively. The whiskers extend to the most extreme data points not considered outliers, and the outliers are plotted individually using the '+' symbol.

The algorithm follows the following steps:

1. When a bond breaks, the energy of all microcracks in the source region is summed to calculate the initial energy of the macrorupture event (E^0). The size of the source region is chosen as 2400 μm , which is three times the diameter of the largest particle in our models [Fig S6a], as recommended by Hazzard and Young [2000].
2. The calculated energy of all new microcracks [Eq. S2] occurring in the source region (W_{frac}) is monitored for the duration of the macrorupture event and added to the energy of the macrorupture event as

$$E_c = E^0 + W_{frac} \quad , \quad (S3)$$

where E_c is the total energy of the a clustered macrorupture event.

3. The event duration is calculated by assuming that each cluster is an expanding shear fracture. Shear fractures propagate as slowly as half the speed of the shear wave velocity of the rock [Madariaga, 1976]; we assume a constant shear wave velocity of 1500 m/s for our sandstone analog (from experimental values of shear wave velocity in Berea Sandstone provided by Mavko et al., 2009). For an initial source dimension of 2400 μm , we calculate a maximum crack propagation duration of 3.2 μs in our numerical sandstone analog [Fig. S6b]. We maintain a time step of 2×10^{-7} s in our simulations, allowing for accurate clustering of microcrack energy in our sandstone analog.

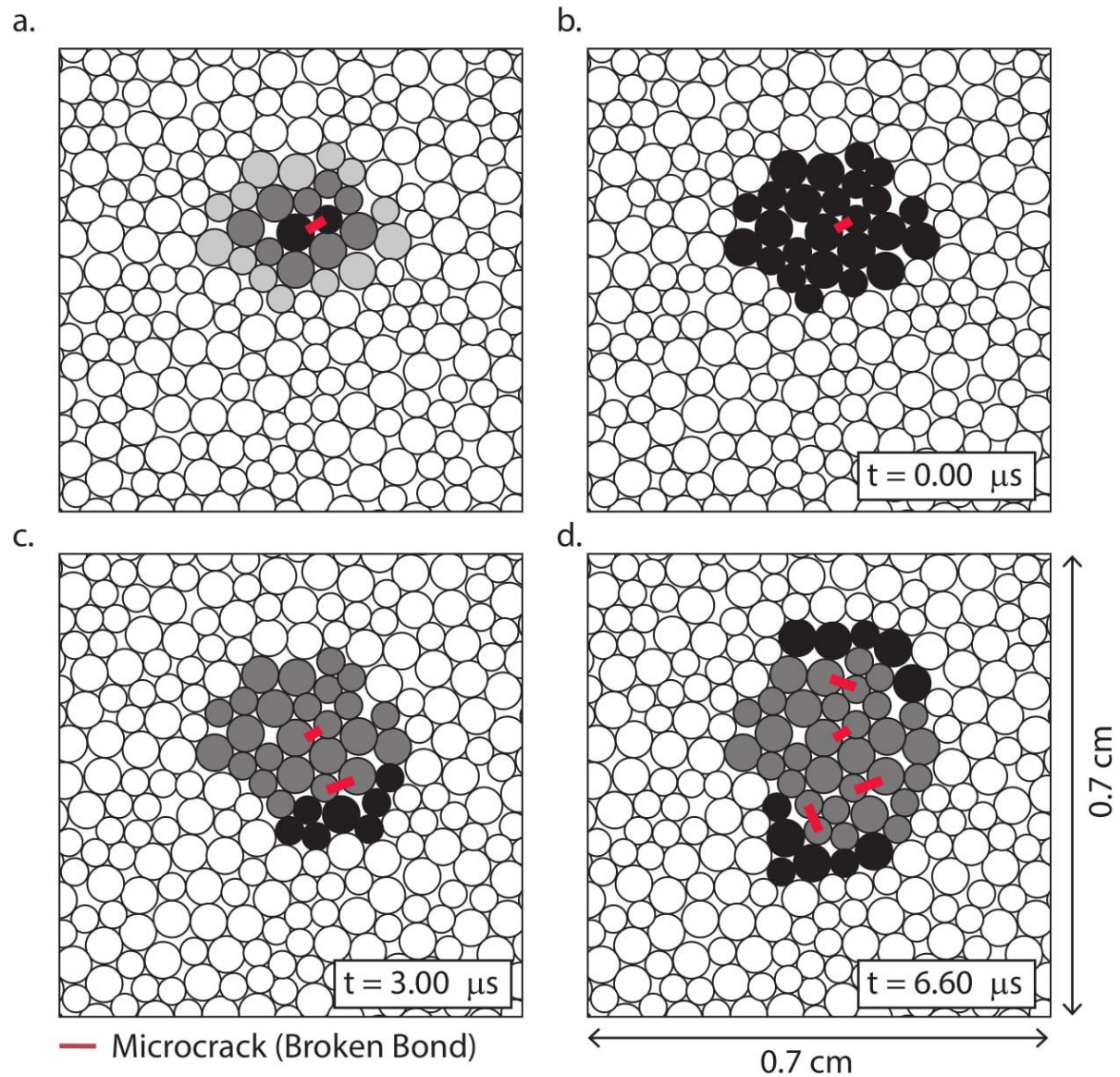
4. If no more microcracks form within the source region over the duration of the event, then the E_c is the maximum energy of a macrorupture event, and the corresponding moment magnitude is calculated as

$$M = \frac{2}{3} \log_{10} E_c - 2.9 \quad . \quad (S4)$$

5. If another crack occurs within the source area before the end of the monitoring period, then it is incorporated into the event. When this happens, the time is set back to zero and source area is

170 expanded to include particles surrounding the new crack. The energy of all particles in the
171 expanded source region is then monitored until the duration of the event has elapsed and no more
172 cracks form within the source area [Fig. S6c,d]. The even magnitude is calculated using Eq. S4.

173 The implemented spatio-temporal clustering of microcrack energy for seismic moment results in a wider
174 range of seismic moments during fracture nucleation and rupture [Fig. 6b], correcting for the limitations
175 of discrete particles of limited size distribution.



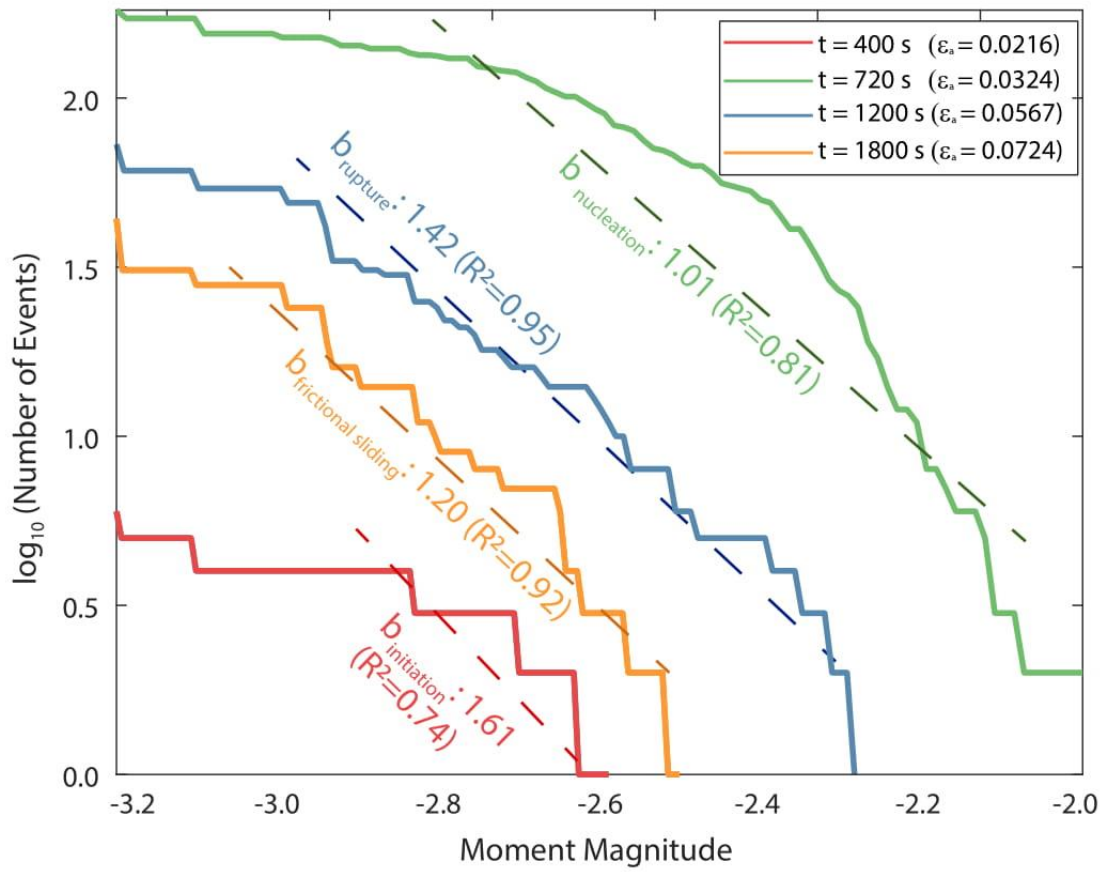
176

177 *Figure S6: AE composed of four microcracks. (a) Particles making up AE source. Black particles are the*
 178 *parent particles formerly connected by a bond, dark grey particles are in contact with parent particles,*
 179 *and light grey particles are in contact with the dark grey particles. (b-d) First, second and third stage of*
 180 *AE composed of four microcracks, each shown by red lines. Time from first bond breakage is shown in*
 181 *each frame. Particles involved in energy calculations are colored in grey. New particles added to the*
 182 *source area after formation of a new microcrack are colored in black.*

Text S2c: Calculation of Seismic b-value

The interpretation of seismic *b-value* within each time window is conducted using guidelines provided by Okal and Romanowicz [1994] and Felzer [2006]. The interpretation of seismic b-value within each time window is conducted in the following steps:

1. We calculate the range of seismic moment (ΔM) as the difference between the largest moment magnitude (M_{max}) and smallest moment magnitude (M_{min}) within each time window.
2. For each time window, we define 100 bins with range ($\Delta M/100$) and develop a cumulative frequency-magnitude histogram that counts the number of seismic moments in all of the bins up to the specified bin [Fig. S7].
3. The seismic b-value for each time window is determined as the slope of the moment frequency-magnitude distribution [Fig. S7]. To interpret the slope of moment frequency-magnitude plot for each time window, we employ consistent magnitude cutoffs of 5% and 95% of ΔM . The lower limit of 5% of ΔM eliminates the influence of small, independent microcracking during b-value interpretation, while the upper limit of 95% of ΔM eliminates the influence of mainshocks on b-value interpretation [Lockner, 1993; Boettcher et al., 2009].
4. We apply a least-squares regression upon the seismic moments lying within 5%-95% of ΔM within each time window. Seismic b-value is interpreted as the slope of the fitted line [Fig. S7].



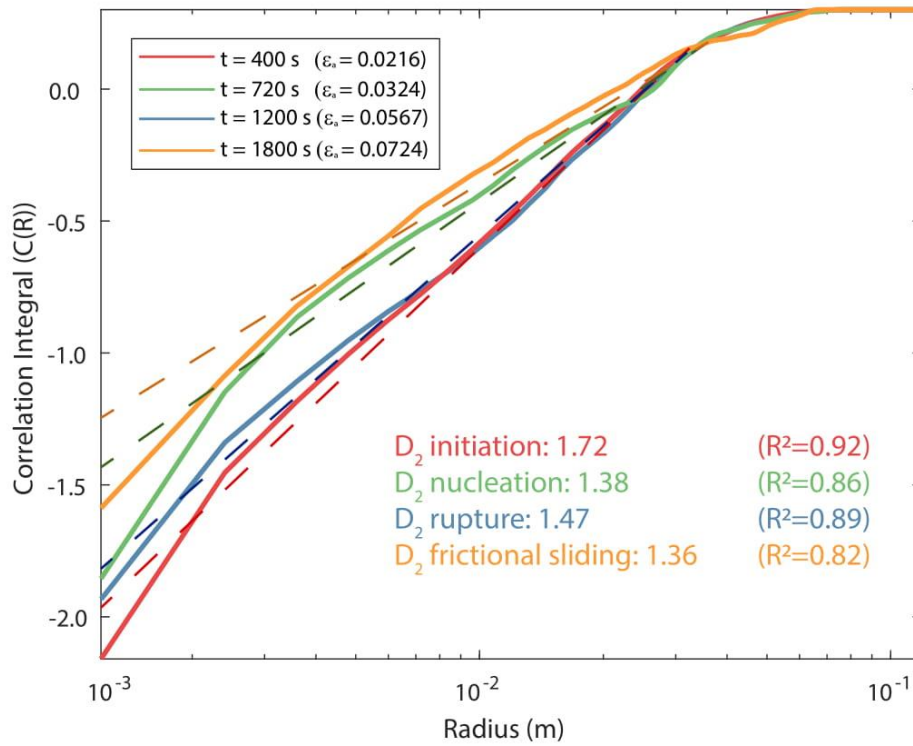
200

201 *Figure S7: Seismic b-values calculated from time windows during the initiation, nucleation, rupture and*
 202 *frictional sliding phase of biaxial test on sandstone analog under confining pressure of 10 MPa. Seismic b-*
 203 *value is calculated as the slope of the moment cumulative frequency-magnitude distribution of clustered*
 204 *microcrack energy. b-values document precursory decline in magnitude during the nucleation phase.*

Text S3: Calculation of Fractal Dimension (D_2)

The correlation exponent, D_2 , is estimated from the slope of a log-log plot of $C(R)$ versus R within each time window [Fig. S8]. The slope of curve $C(R)$ versus R is estimated using linear regression where slope of the curve is maintained greater than zero (eliminating constant values of $C(R)$) [Fig. S8]. The interpretation of the fractal dimension is conducted based on guidelines described by Bonnet et al. [2001]:

- The maximum value of R is chosen as the length of the simulated sandstone sample, providing a statistically acceptable representation of microcracking across the area of the sample [Fig S8].
- The value of $C(R)$ is calculated over 2-3 orders of magnitude of R , providing for good definition of the exponent D_2 [Fig S8].



214

215 *Figure S8: Fractal Dimension (D_2) calculated as the slope of the correlation integral ($C(R)$) and radius*
 216 *(R). D_2 calculated during time windows at $t= 400$ s, 720 s, 1200 s and 1800 s respectively, corresponding*
 217 *to strain markers 1-4 in Fig. 1 and Fig. 2 during biaxial test on sandstone analog under confining*
 218 *pressure of 10 MPa.*

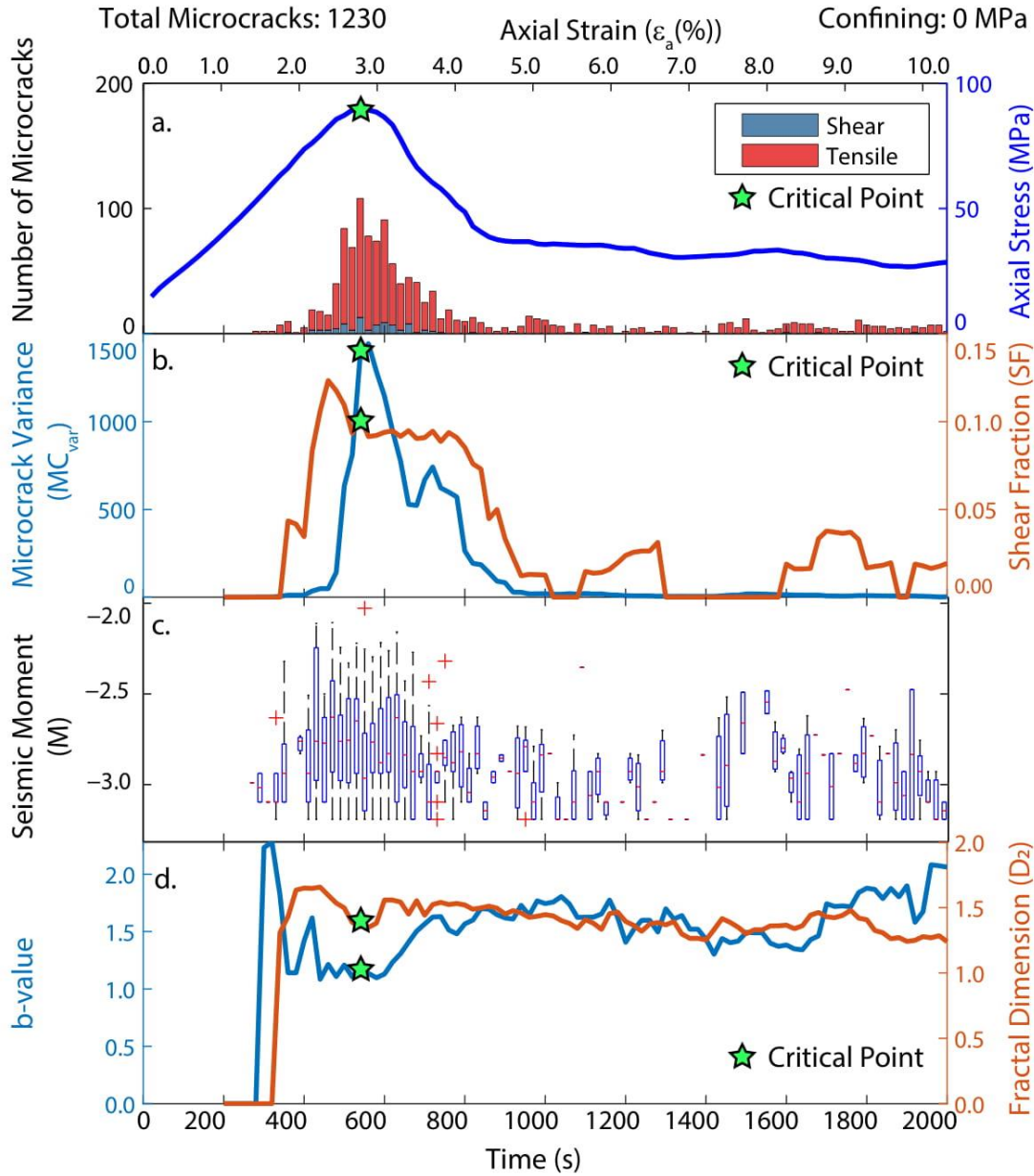


Figure S9: Evolution of microcracking and deformation indicators in sandstone analog during biaxial test under confining pressure of 0 MPa. (a) Applied axial stress and microcracking in shear and tensile modes documented as a function of axial strain. (b) Indicators microcrack variance (MC_{var}) and shear fraction (SF) exhibit precursory increase in magnitude prior to critical failure (c) Calculated increase in range of seismic moment magnitudes prior to critical failure. On each box, the central mark indicates the median moment magnitude, box indicates the 25th and 75th percentiles, respectively, whiskers extend to the most extreme data points not considered statistical outliers, and outliers are plotted individually using the '+' symbol. (d) Deformation indicators seismic b-value and fractal dimension of microcrack location (D_2) exhibit precursory decline prior to critical failure.

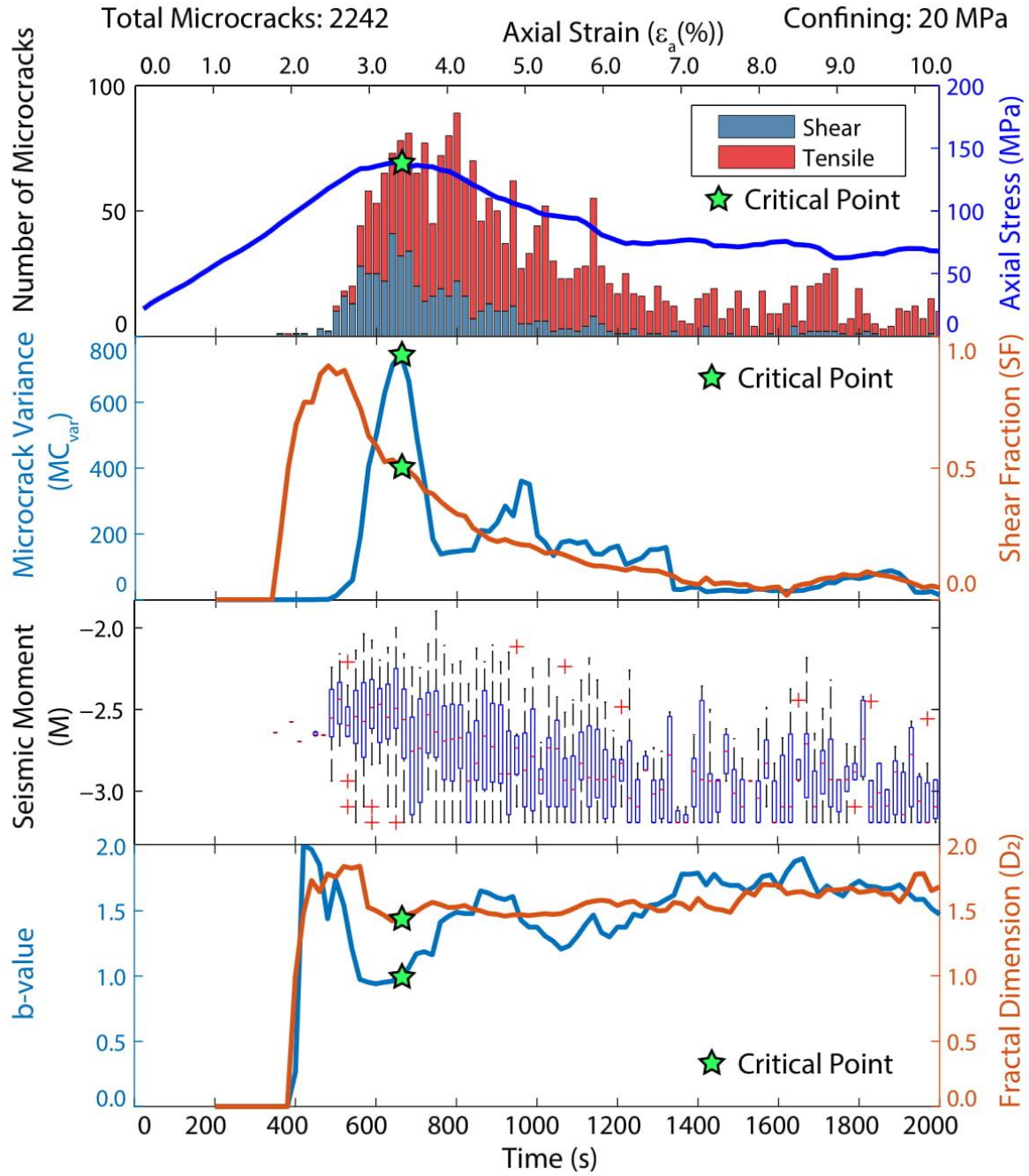
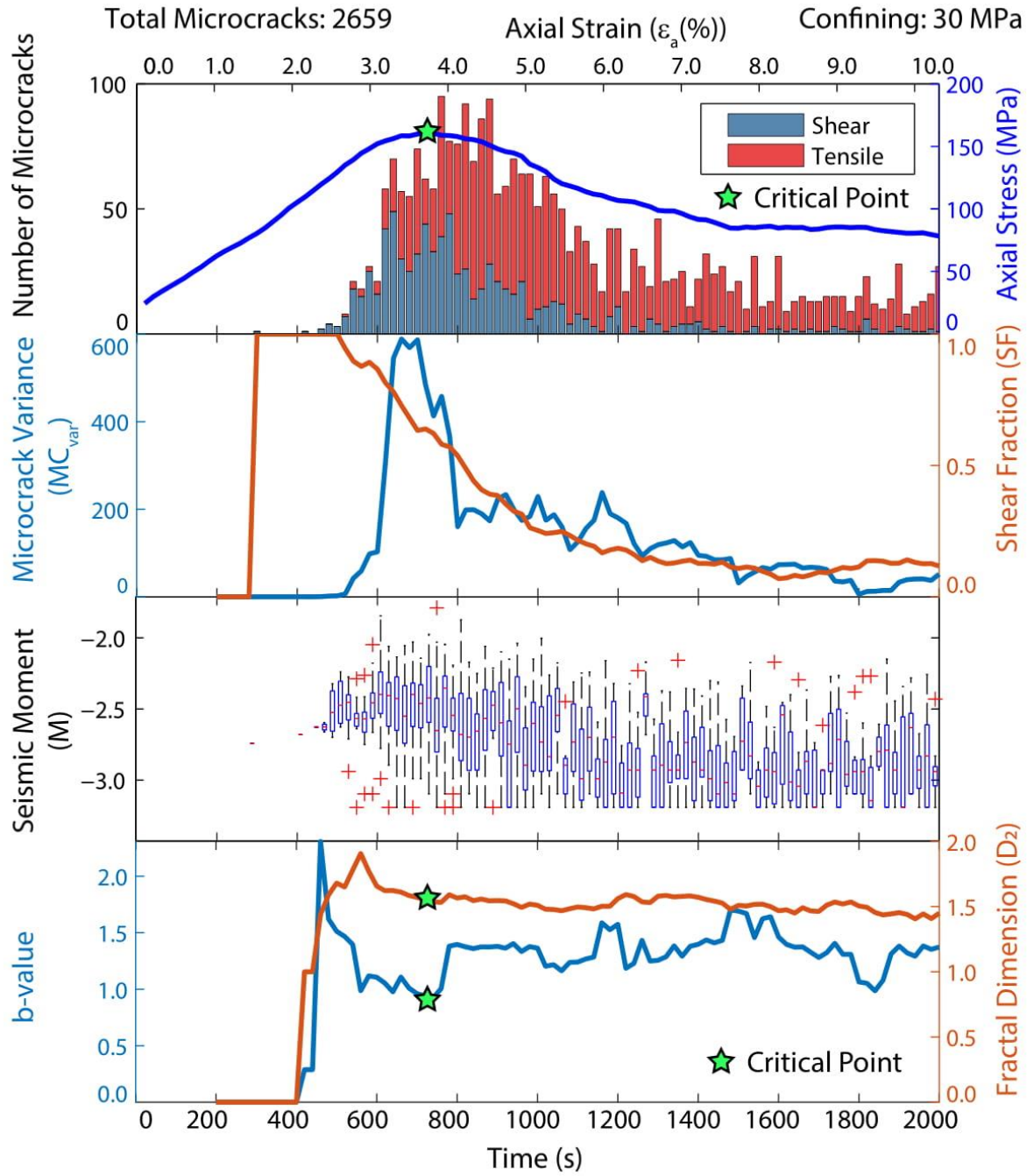
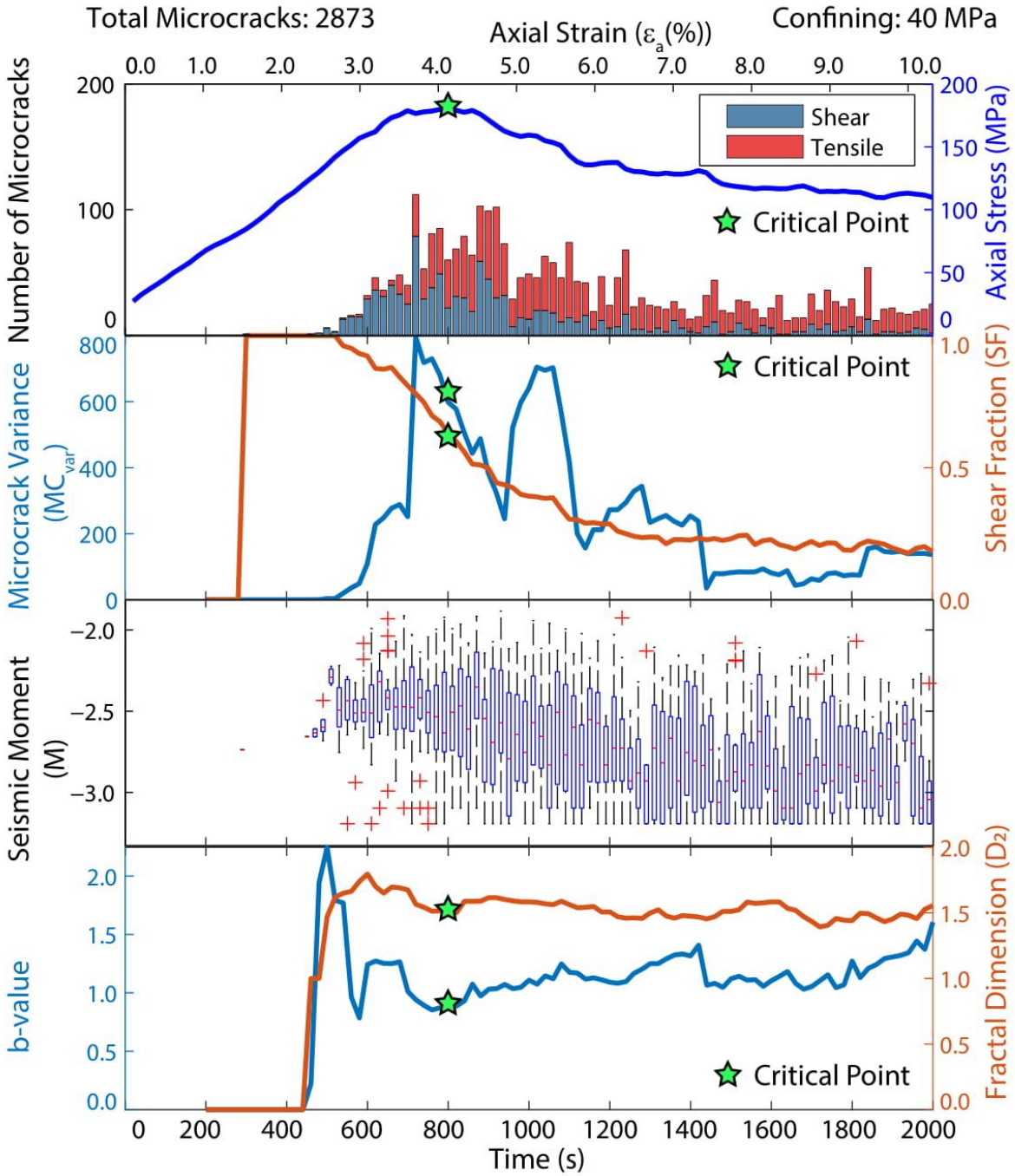


Figure S10: Evolution of microcracking and deformation indicators in sandstone analog during biaxial test under confining pressure of 20 MPa. (a) through (d) same as in Figure S10.



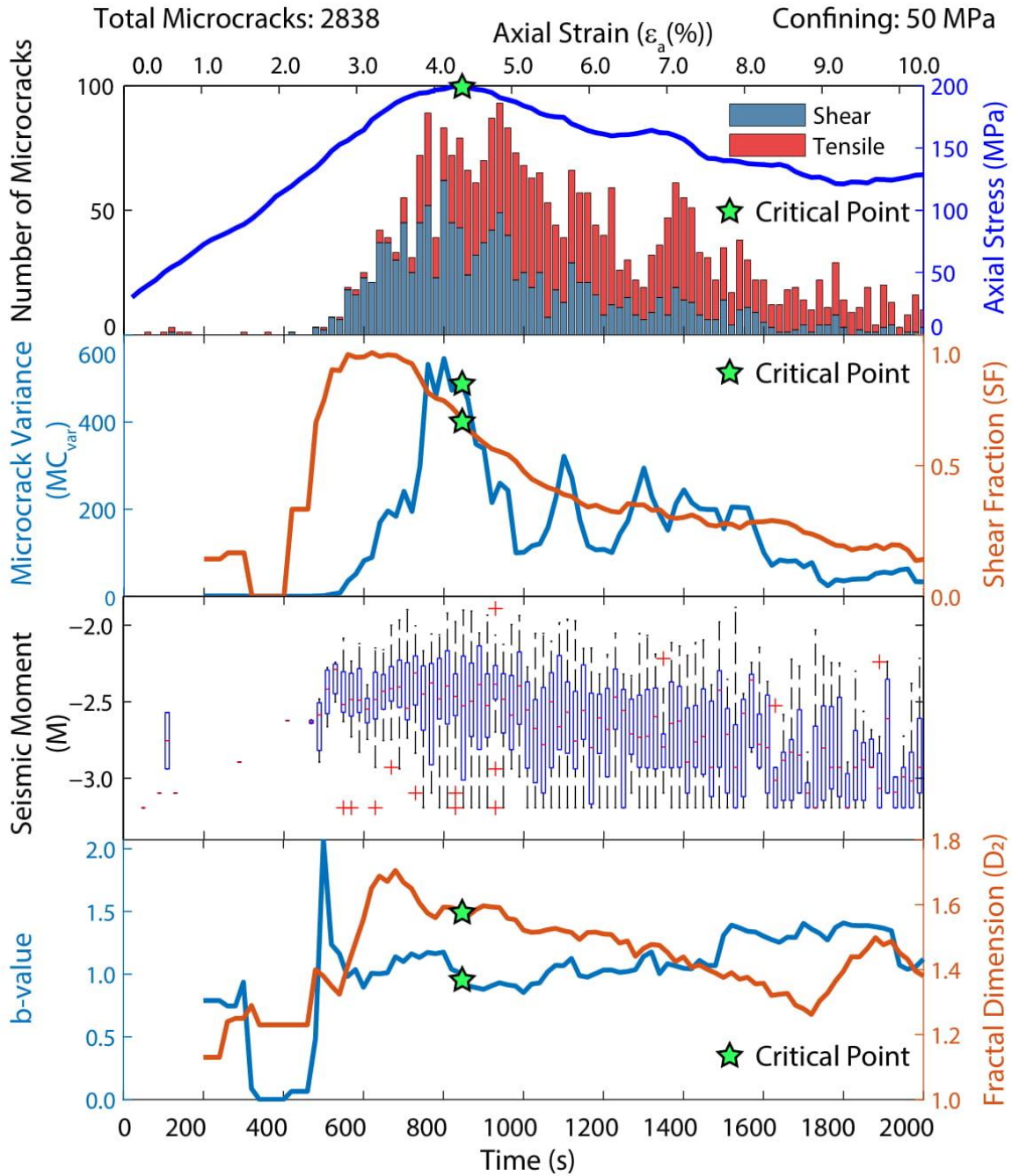
233

234 *Figure S11: Evolution of microcracking and deformation indicators in sandstone analog during biaxial*
 235 *test under confining pressure of 30 MPa. (a) through (d) same as in Figure S10.*



236

237 *Figure S12: Evolution of microcracking and deformation indicators in sandstone analog during biaxial*
 238 *test under confining pressure of 40 MPa. (a) through (d) same as in Figure S10.*



239

240

241

Figure S13: Evolution of microcracking and deformation indicators in sandstone analog during biaxial test under confining pressure of 50 MPa. (a) through (d) same as in Figure S10.

Text S4: Details of Multilayer Perceptron (MLP)

S4a: Architecture of the Multilayer Perceptron (MLP)

The MLP correlates using an arbitrary function between input deformation indicators with target values, time-to-failure (*TTF*) and stress-to-failure (*STF*), through iteratively application synaptic weights (w_{xy} and w_{yz}) [Fig. S15]. In a multi-layer perceptron, each layer computes a vector function in the form:

$$z = g(W^T x + b) \quad (\text{Eq. S5})$$

Where $z \in R^N$ is a vector of activations of the nodes of the hidden layer, with N nodes; $x \in R^M$ is a vector of the activations of nodes of the previous layer, with M nodes, $W \in R^{M \times N}$ is a matrix of weights linking nodes in x and z ; $b \in R^N$ is a vector of biases for layer z ; and $g(*)$ is an element wise non-linear function, known as the activation function. The non-linear activation function allows for the neural network to approximate arbitrary functions [Goodfellow et al., 2016]. Common activation functions used in geophysical work include logistic sigmoid, hyperbolic tangent, rectified linear unit (ReLU) [van der Baan and Jutten, 2000; Goodfellow et al., 2016]. Since there is no easy rule to determine the optimum architecture of a neural network, we evaluate the performance of the MLP by varying number of neurons in the hidden layer and activation functions [Basheer and Hajmeer, 2000]. We choose the hyperbolic tangent activation function ($g(z) = 2/(1 + \exp(-2 * z)) - 1$) and five hidden neurons ($m=5$) in our study as it yields good performance with a simple architecture [Fig. S15].

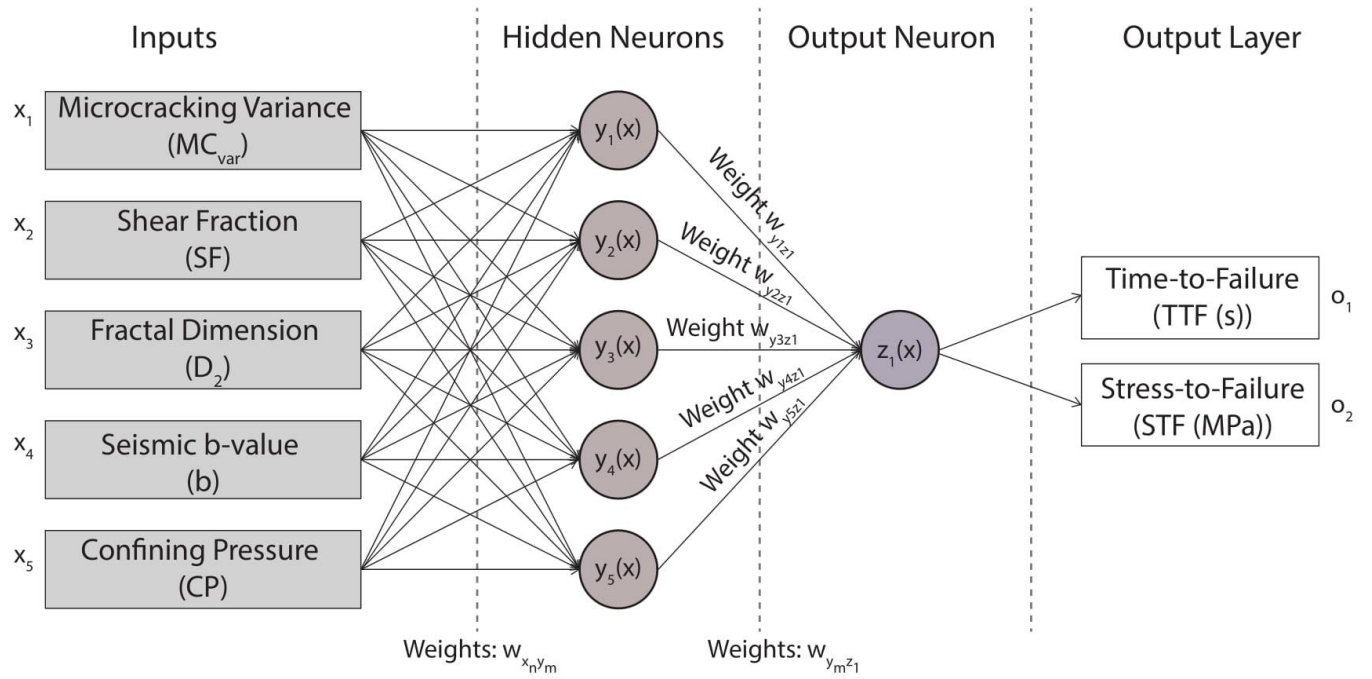
S4b: Training and Testing of the Multilayer Perceptron (MLP)

The rows of input matrix correspond to 91 time windows for nine individual biaxial tests ($91 \times 9 = 819$ rows). The columns of the array are confining pressure (*CP*) and deformation indicators microcracking variance (MC_{var}), shear fraction (*SF*), seismic *b-value* and fractal dimension (D_2) [Fig. S14]. We randomly allocate 70% of this dataset as training dataset and the remaining 30% as testing dataset. All data were normalized so each feature would be in the range of [0, 1] before training, preventing the network from

265 favoring one input feature over others [Goodfellow et al., 2016]. The MLP is first trained on the training
266 dataset: in this phase the MLP learns the relationships between data features and the targets *TTF* and *STF*.
267 The objective function for regression tasks in our MLP is the MSE-Squared-Error (*MSE*), defined as the
268 average squared difference between the neural network prediction and the true target,

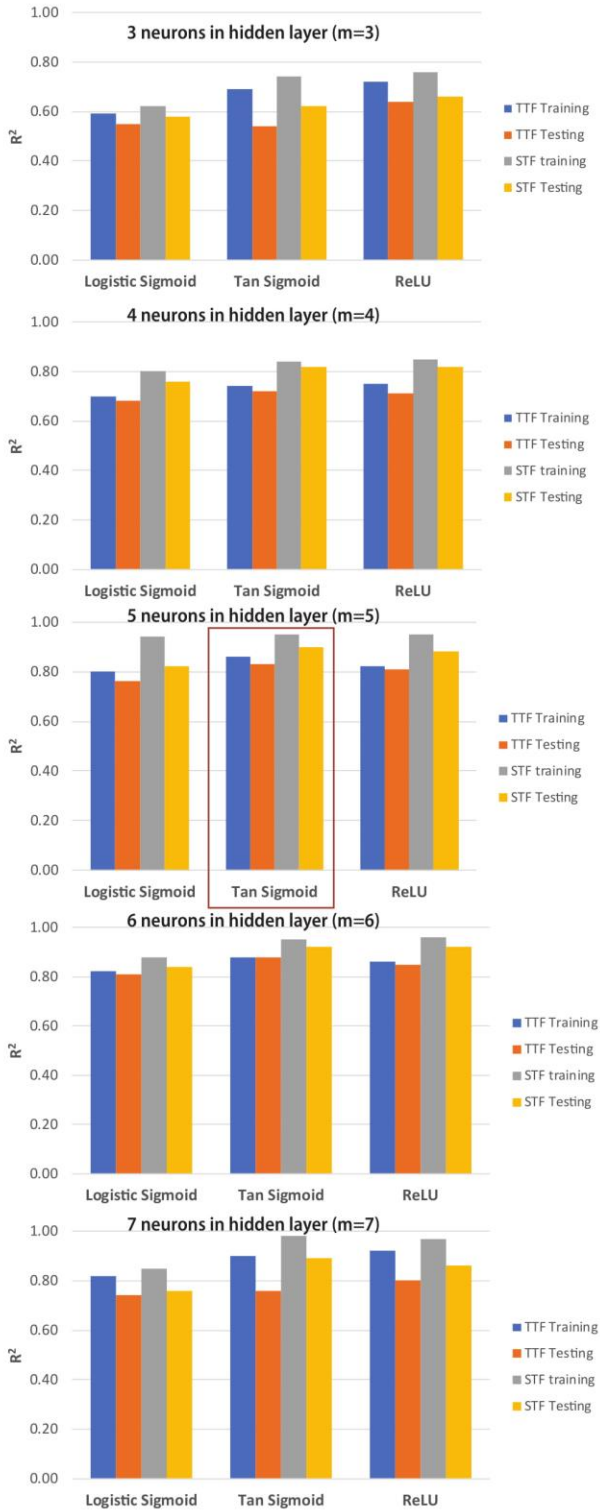
$$269 \quad MSE = \frac{1}{N} \sum_{i=1}^N |y_i - \bar{y}_i|^2 \quad , \quad (Eq. S6)$$

270 where y_i and \bar{y}_i are the estimated value and known value for example i , and N is the number of training
271 examples. The goal of the MLP is to minimize *MSE* on the training dataset, which is a set of inputs
272 (deformation indicators and confining pressure) with known target values (*TTF* and *STF*) using gradient
273 descent [Goodfellow et al, 2016]. Thus, the MLP trains by iteratively varying connection weights w_{xy} and
274 w_{yz} to optimize fit to desired target values (*TTF* and *STF*) using the gradient descent algorithm to attain
275 the lowest possible value of MSE [Goodfellow et al., 2016] [Fig. 3]. The trained MLP is then fed with
276 testing dataset and predicts values for *TTF* and *STF* [Fig. 3].



277

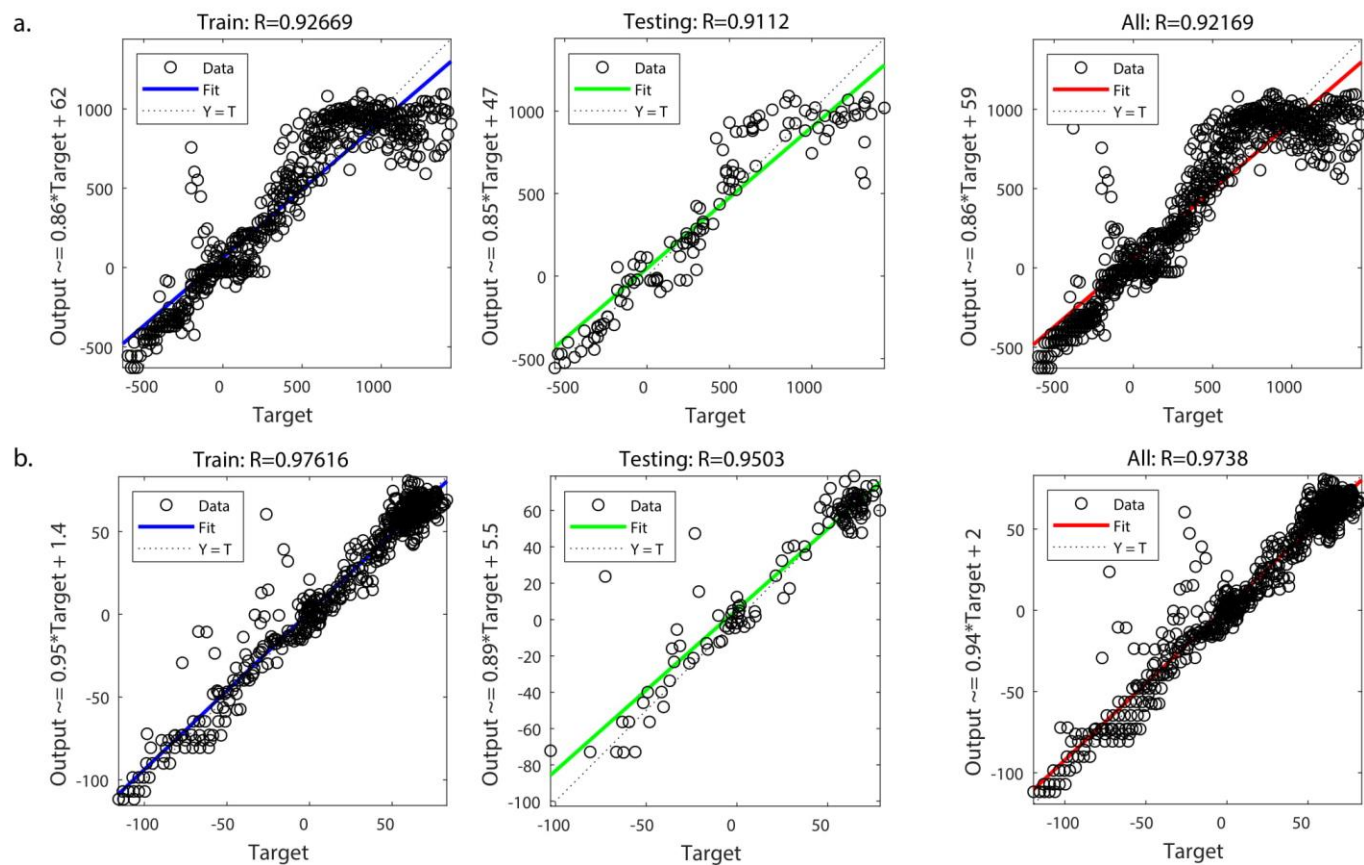
278 *Figure S14: Architecture of Multilayer Perceptron (MLP) employed in our study to predict critical failure*
 279 *in sandstone analog during biaxial tests under confining pressures of 0-50 MPa.*



280

281 *Figure S15: Regression performance during testing and training for TTF and STF predictions using*
 282 *varying activation functions and number of hidden neurons in MLP. We employ the tan sigmoid*
 283 *activation function and five neurons in the hidden layer as it yields good performance and low training*
 284 *time for MLP.*

285 **Figure S16: Regression Performance of MLP**



286

287 *Figure S16: Regression performance during training (left panel), testing (center panel) and overall*
 288 *dataset (right panel) using MLP for (a) Time-to-failure predictions (TTF), and (b) Stress-to-failure (STF)*
 289 *predictions.*

290 *Table S3: Relative Importance of Input Deformation Indicators for Time-to-Failure predictions using*
291 *MLP network reveals MC_{var} and D_2 as primary predictors.*

Input Layer-Hidden Layer					
	Input 1: Confining Pressure (CP)	Input 2: Microcracking Variance (MC_{var})	Input 3: Shear Fraction (SF)	Input 4: Fractal Dimension (D_2)	Input 5: Seismic b-value
Neuron y_1	-2.914	-1.790	-0.167	0.491	-1.107
Neuron y_2	-0.826	-0.258	1.606	-1.784	-0.993
Neuron y_3	-0.889	3.846	2.404	0.587	2.298
Neuron y_4	0.558	-0.057	1.432	2.950	3.181
Neuron y_5	0.097	5.691	0.466	0.519	2.308
Hidden Layer – Output Layer					
Neuron z_1	0.126	0.101	-0.766	0.824	0.269
Connection Weights and Relative Importance					
Neuron y_1-z_1	0.451	0.277	0.026	0.076	0.171
Neuron y_2-z_1	0.151	0.047	0.294	0.326	0.182
Neuron y_3-z_1	0.089	0.384	0.240	0.059	0.229
Neuron y_4-z_1	0.068	0.007	0.175	0.361	0.389
Neuron y_5-z_1	0.011	0.627	0.051	0.057	0.254
Sum	0.769	1.341	0.786	0.879	1.225
Relative Importance (%)	15.384	26.826	15.716	17.571	24.502
Rank	5	1	4	3	2

293 *Table S4: Relative Importance of Input Deformation Indicators for Stress-to-Failure predictions using MLP*
294 *network reveals SF and b-value as primary predictors.*

Input Layer-Hidden Layer					
	Input 1: Confining Pressure (CP)	Input 2: Microcracking Variance (MC_{var})	Input 3: Shear Fraction (SF)	Input 4: Fractal Dimension (D₂)	Input 5: Seismic b-value
Neuron y ₁	0.298	-2.763	0.822	-2.328	0.714
Neuron y ₂	-1.199	1.674	5.259	-2.537	3.423
Neuron y ₃	0.911	-0.477	-1.750	-0.541	-1.558
Neuron y ₄	0.192	-0.494	-2.528	-4.188	2.018
Neuron y ₅	0.165	-0.657	-0.195	-0.163	-0.444
Hidden Layer – Output Layer					
Neuron z ₁	0.098	-0.267	0.384	0.117	-2.298
Connection Weights and Relative Importance					
Neuron y ₁ -z ₁	0.043	0.399	0.119	0.336	0.103
Neuron y ₂ -z ₁	0.085	0.119	0.373	0.180	0.243
Neuron y ₃ -z ₁	0.174	0.091	0.334	0.103	0.297
Neuron y ₄ -z ₁	0.020	0.052	0.268	0.445	0.214
Neuron y ₅ -z ₁	0.101	0.405	0.120	0.100	0.273
Sum	0.424	1.066	1.215	1.165	1.131
Relative Importance (%)	8.476	21.319	24.297	23.290	22.618
Rank	5	4	1	2	3